Atomic Structure Modification for Electrochemical Nitrogen Reduction to Ammonia

Xinrui Chen, Yitian Guo, Xinchuan Du, Yushuang Zeng, Junwei Chu, Chuanhui Gong, Jianwen Huang,* Cong Fan, Xianfu Wang,* and Jie Xiong*

The electrochemical nitrogen reduction reaction (NRR), as an environmentally friendly method to convert nitrogen to ammonia at ambient temperature and pressure, has attracted the attention of numerous researchers. However, when compared with industrial production, electrochemical NRR often suffers from unsatisfactory yields and poor Faraday efficiency (FE). Recently, various structure engineering strategies have aimed to introduce extra active sites or enhance intrinsic activity to optimize the activation and hydrogenation of N_2. In this review, recent progress in atomic structure modification is summarized and discussed to design high-efficiency NRR catalysts, with a focus on defect engineering (heteroatom doping and atom vacancy), surface orientation and amorphization, as well as heterostructure engineering. In addition, existing challenges and future development directions are proposed to obtain more credible NRR catalysts with high catalytic performance and selectivity.

1. Introduction

With the increasingly prominent energy crisis and environmental degradation caused by the depletion of exhaustible fossil fuels and excessive emission of greenhouse gases, it is imperative to find new clean energy resources with abundant reserves to gradually replace the fossil fuels for future development. As a clean energy carrier, ammonia has great potential due to its high energy density, eco-friendly combustion products, abundant raw material of N_2 in atmosphere, and, especially, widespread applications in industry and agriculture. Currently, the industrial ammonia production from N_2 mainly adopts the Haber–Bosch method under high temperature (350–550 °C)

and high pressure (15–30 MPa),[1,2] which consumes more than 1% of the energy generated in the world each year.[3] This is due to the high bond energy of N≡N bond (941 kJ mol⁻¹), especially the first step cleavage that requires thermodynamically strong energy barrier of 410 kJ mol⁻¹. To maintain the reaction, it is necessary to artificially input massive energy to activate the strong bonding. Therefore, an efficient ammonia preparation process with relatively low energy consumption, low pollution, and mild conditions is urgently needed.

Methods based on electrochemical catalytic reactions such as hydrogen evolution reaction (HER), oxygen evolution reaction (OER), carbon dioxide reduction reaction (CO_2RR), and oxygen reduction reaction (ORR) have achieved great progress in the preparation of hydrogen,[4–8] hydrocarbons,[9] and oxygenates,[10] which also meet the basic requirements for establishing an emerging ammonia production process. Therefore, the study on electrochemical nitrogen reduction reaction, including reaction mechanism and electrocatalyst design, has become a top priority. In nature, the biological nitrogenase can convert N_2 into NH_3 under normal temperature and pressure. The iron–molybdenum cofactor based on the nitrogenase C@Fe_6MoS_9 cluster with complexation and reduction active sites is considered to be the intrinsic complex for the nitrogen fixation.[11] Therefore, a large number of electrocatalysts with similar mechanisms such as transition metal sulfides and nitrides are successively analyzed and optimized, exhibiting good nitrogen-fixing properties.[12–15] In addition, some studies further developed materials like B_4C, Bi, and black phosphorus for electrocatalytic nitrogen fixation due to the similarities in the properties of elemental electron orbital structures when compared with transition metals.[16–19]

In spite of the great progress on the catalysts for NRR, regrettably, almost all electrocatalysts developed have not been exhibiting significant yields and Faraday efficiency (FE) for industrialization, mainly due to the competition between NRR and HER. In general, electrocatalysts with abundant active sites exposed at the interface between electrolyte and materials facilitate the adsorption and activation of N_2. The electrolyte, however, a natural proton source, can enable more protons during reaction due to the lower activation energy when compared with that for N_2, that is, active sites on the interface are preferentially

X. Chen, Y. Guo, X. Du, Y. Zeng, J. Chu, C. Gong, J. Huang,
Prof. X. Wang, Prof. J. Xiong
State Key Laboratory of Electronic Thin Films and Integrated Devices
University of Electronic Science and Technology of China
Chengdu 610054, China
E-mail: huacrystalring@gmail.com; xfwang87@uestc.edu.cn;
jiexiong@uestc.edu.cn
C. Fan
School of Materials and Energy
University of Electronic Science and Technology of China
Chengdu 610054, China

**ADVANCED
SCIENCE NEWS**
www.advancedsciencenews.com

**ADVANCED
ENERGY
MATERIALS**
www.advenergymat.de

occupied by protons first rather than N_2. Hence, the number of active sites for electrochemical NRR is reduced, so that most of the proton and electron transports contribute to HER, not NRR. In short, in order to alleviate the inhibitory effect of HER on NRR, it is available to slow down the transfer of protons from the electrolyte to the catalyst surface by selecting, designing, and engineering electrocatalysts, thereby promoting NRR.

In this review, we will introduce the development of electrocatalytic nitrogen fixation under mild conditions from theoretical and experimental perspectives, respectively. We begin with the introduction of the three reaction pathways for the conversion from N_2 to NH_3 at the catalyst/electrolyte interface, combining with calculation analysis to reveal the rate-determining step for deciding which reaction pathway can be carried out continuously. Section 2 is mainly about the recent advances in various material design strategies containing defect engineering, surface orientation and amorphization, as well as heterostructure engineering in electrochemical NRR, impacts and shortcomings of which are discussed in detail. Finally, challenges and outlooks in electrocatalytic nitrogen fixation are briefly summarized for future exploration.

2. Fundamental Principles of Electrochemical NRR

The reaction mechanism of NRR is usually divided into two kinds: dissociative and associative mechanisms (**Figure 1**).[20] During the dissociative pathway, the N≡N triple bond is first cleaved, then two independent N atoms are adsorbed on the surface of the catalyst followed with being hydrogenated. This mechanism usually occurs at the Haber–Bosch process, where harsh conditions are essential. While for the associative mechanism, the step of adding H atoms to N atom is completed before the cleavage of N≡N bond. According to the different hydrogenation sequence, the associative mechanism can be further divided into distal and alternating pathways. In the distal pathway, the distal N atom away from the adsorption site first acquires H continuously to form NH_3. After the first NH_3 released, the other N atom begins to proceed with the hydrogenation process. In the alternating pathway, the H atoms are alternately bonded with both N atoms. At the end of the reaction, two NH_3 molecules are released. During all these three pathways, only one N atom of the nitrogen molecule is adsorbed on the active site, namely, end-on configuration. Another pathway is the enzyme catalysis, which also involves an alternating hydrogenation process, but both N atoms are adsorbed on the active sites to form the side-on configuration. The conversion from nitrogen to ammonia undergoes multi-step proton–electron transfer, and different intermediates are produced in each reaction pathway.[21]

Considering that NRR involves multiple intermediates, theoretical calculations are often used for detailed analysis of the reaction process. For example, Nørskov's group carried out density functional theory (DFT) calculations to estimate the free energy of the intermediates in NRR.[22] They confirmed that the multiple reaction steps of NRR are not isolated from each other, but mutually constrained, and there are linear scaling relations between the various intermediate steps, so it is possible to use only one descriptor of the N* binding energy to exhibit the
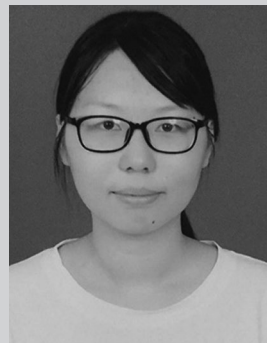
Xinrui Chen is currently perusing her B.S. degree and will be a Ph.D. student under the supervision of Prof. Jie Xiong at University of Electronic Science and Technology of China (UESTC). Her research focuses on the design and synthesis of function materials for energy storage.
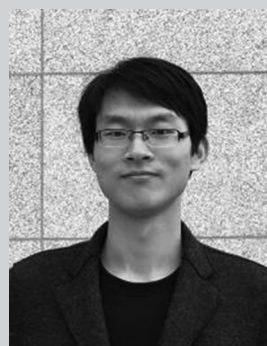
Jianwen Huang received his B.S. degree at UESTC in 2014. He is currently a Ph.D. student supervised by Prof. Yanrong Li. His research interests are the design of materials and structure for energy conversion and storage.

Jie Xiong is a full Professor at UESTC. He received his Ph.D. degree in materials physics and chemistry from UESTC in 2007, and went to Los Alamos National Laboratory for his postdoctoral research from 2009 to 2011. His research interests have focused on the synthesis–structure–property mechanism of functional nanomaterials and energy materials and their applications in energy science, electronics, and optoelectronics.

catalytic performances.[23] Considering the ability of the transition metal (TM) to activate the N≡N triple bond by the acceptance and back-donation process, they established volcanoes of overpotential and N* binding energy of various transition metals. The acceptance and back donation of electrons is a typical phenomenon that often occurs between TM and N_2 molecules.[24] The empty orbital of TM can accept the lone-pair electrons of nitrogen, and then donate the electrons into the antibonding orbital of nitrogen to activate the N≡N triple bond. They found only the catalysts with moderate N* binding energy show superior catalytic activity, while the larger the difference between the two volcanoes of NRR and HER, the better the selectivity.

Giving the fierce competition between NRR and HER, the design strategy of the catalyst with high FE and NH_3 yield is usually considered from two aspects: i) improving the intrinsic
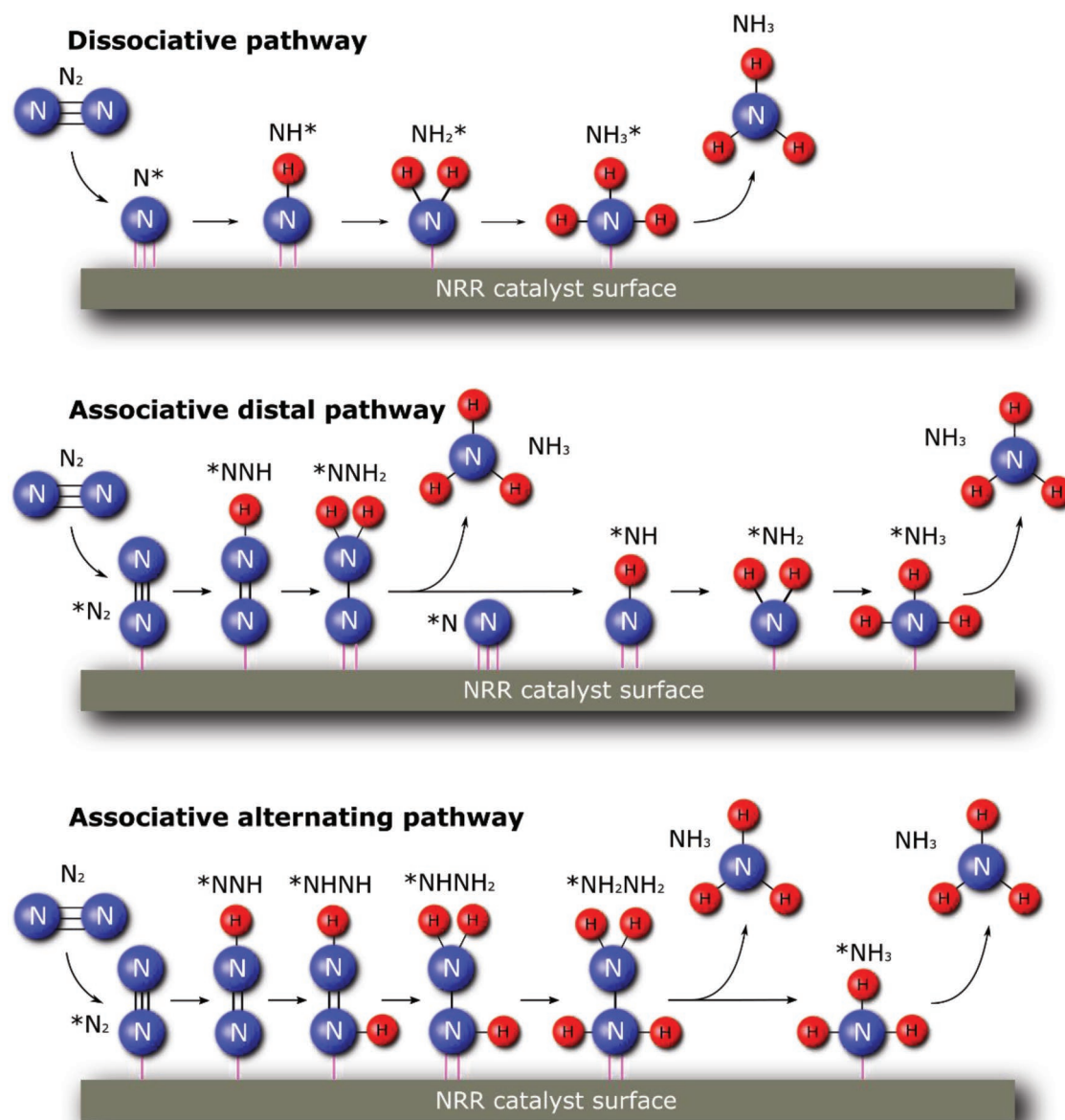
Figure 1. The possible reaction mechanism of NRR including dissociative pathway, associative distal, and alternating pathways. * represents an adsorption site.

catalytic performance of NRR; ii) strengthening the suppression of HER. In recent years, lots of strategies have been proposed and developed to engineer the NRR activities of the designed electrocatalysts with enhanced FE and NH_3 yield. In the following content, we summarize the well-designed novel strategies for catalysts in several aspects of defect engineering, surface orientation and amorphization, as well as heterostructures.

3. Defect Engineering

Based on the principle of NRR, the tactic of fabricating various defects is an effective and reliable mean to improve the catalytic

performance by adjusting the intrinsic properties of the electrocatalysts. To unveil the detailed mechanisms of the defect-engineered NRR activities of the catalysts, two representative cases of heteroatom doping and atomic vacancy are selected for the full discussion.

3.1. Heteroatom Doping

Introducing the exotic atoms (heteroatom doping) can advantageously increase the active sites and reduce the energy barrier for the rate-determining step of NRR by forming the extraordinary coordination environment and electronic structure. Therefore, heteroatom doping as a very effective strategy has

ADVANCED
SCIENCE NEWS
www.advancedsciencenews.com

ADVANCED
ENERGY
MATERIALS
www.advenergymat.de

been exhaustively studied to improve the activity of the electro-catalytic materials. Currently, the field of heteroatom doping for NRR grows very fast. In this section, we review the progress of heteroatom doping in very recent years from the perspectives of detailed mechanism and NRR performance.

3.1.1. Metal-Atom Doping

Basically, two kinds of metal-atom doping are well developed. One is using an atomic-scale-dispersion dopant to form the single-metal-atom catalysts (SMACs) or double-metal-atom catalysts (DMACs), since the resulting SMACs and DMACs can tremendously increase the atom utilization and significantly lower the material price. For clarity, the other strategy to realize the metal-atom-tailored catalysts is called the non-atomic-scale-dispersion doping.

In 2011, the first example of SMACs was clearly reported by Zhang's group, where the single-atom Pt was doped into FeO_x.[25] Notably, the $Pt@FeO_x$ complex could not be applied for NRR. In 2018, several groups made the quantum calculation by constructing the models of SMACs. For example, Li's group constructed several SMACs by doping various TM atoms (such as Pt, Ru, and V) into the 2D $g-C_3N_4$ with N vacancies ($TM@g-C_3N_4$).[26] Due to the calculated lowest energy barrier (0.57 eV), the model of $Ti@g-C_3N_4$ was predicted to exhibit the best NRR performance. Meanwhile, Ma and co-workers predicted that the Fe-doped monolayer phosphorene (Fe@P) SMAC could exhibit better catalytic performance than the original matrix using the spin-polarized DFT.[27] In their results, the Fe@P complex exhibited an exotherm when N_2 is absorbed, indicating the sufficient activation of N_2. Importantly, the doped Fe atom not only reduced the bandgap of the complex to 0.65 eV, quickening the charge-transfer process, but also acted as the catalytic active center for NRR as evidenced by the asymmetric charge and spin-density distribution (**Figure 2**a). Wang's group conducted the theoretical calculations for Mo doping into the N-doped carbon substrates, in which one of the configurations, called the $Mo_1@N_1C_2$ (Figure 2b), was found to has a reasonably low overpotential (0.24 V) for NRR at room temperature due to the distinct metallicity confirmed using the Bader charge analysis (Figure 2c).[28] For the practical concerns, Choi et al. constructed the models of TMs on the defected graphene from the perspective of suppressing HER, where the calculation results indicated the highly unstable *H and *NH_2 formed on the proposed models could suppress the HER process.[29] Interestingly, they pointed out that the models of the N-defected graphene with a single Ti/V atom are the most suitable catalysts. Besides the calculations for SMACs, Jiang's group compared the catalysis difference between SMACs and DMACs by modeling the transition metals (including Cr, Mn, Fe, Co, and Ni) doped into the 2D C_2N using DFT calculations.[30] As demonstrated, all DMACs have lower potentials due to the more favorable bridge sites for N_2 adsorption and much quicker electron-transfer process. Among them, the $Mn_2–C_2N$ complex exhibited the lowest potential (−0.23 V).

Supported by the calculation predictions, many groups synthesized the SMACs and tested their catalytic NRR performance. In 2018, Geng et al. fabricated the Ru@N-doped carbon SMAC (Ru SAs/N–C) by the pyrolysis of zeolitic imidazolate frameworks (ZIF-8).[31] As shown in Figure 2d,e, compared with the Ru nanoparticles (NPs) anchored on NC (Ru NPs/N–C, about 15%, 60 µg h$^{−1}$ mg$_{cat}$$^{−1}$), the resulting Ru SAs/N–C complex exhibited the significantly promoted FE of 29.6% which was stable in three types of electrolyte and a NH_3 yield rate of 120.9 µg h$^{−1}$ mg$_{cat}$$^{−1}$. Furthermore, a distal pathway was confirmed for the hybrid catalyst by calculating the free energy of the reaction (Figure 2f). Sun's group modified the Ru single atom–based complex by doping the Ru atom into the mixed matrix of ZrO_2 and N-doped carbon ($Ru@ZrO_2/NC$), delivering a significantly improved NH_3 yield of 3.665 mg h$^{−1}$ mg$_{cat}$$^{−1}$ (−0.21 V vs reversible hydrogen electrode (RHE)) and an FE of 21% (−0.17 V).[32] In the following, all overpotentials are relative to the standard RHE unless otherwise specified. The enhanced electrocatalytic performance of $Ru@ZrO_2/NC$ was attributed to the lowered free energies in the reaction due to the coexistence of Ru and ZrO_2. At the same time, Adzic and co-workers synthesized a novel SMAC by doping Mo atom into N-doped 3D porous carbon (NPC) (Mo@NPC) as shown in Figure 2g.[33] Successful induction of single atoms can be verified by extended X-ray absorption fine structure (EXAFS) spectra. The Mo@NPC complex with an optimal Mo loading of 9.54% (Figure 2h) exhibited a high NH_3 yield of 34.0 ± 3.6 µg h$^{−1}$ mg$_{cat}$$^{−1}$ and a superior FE of 14.6 ± 1.6% in the alkaline electrolyte, showing negligible activity decay during the 50 000 s testing. They found that the Mo–N sites not only activated the N_2 molecule to stabilize −N_2H species, but also promoted the evolution of −NH_2 species.

Apart from the above doping, the nonatomic-scale-dispersion-doping strategy was also widely adopted. In 2017, Zhang and co-workers made the calculations by modeling Fe doped into the matrix of MoN_2 ($Fe@MoN_2$) and then predicted its electrocatalytic performance.[34] They found that the tetra-coordinate Fe could form a high spin state of t_{2g}-state and thus provided more valence electrons than Mo. Therefore, the N-containing species could be reduced more easily. At the same time, Azofra et al. constructed a model by doping Fe into MoS_2 to simulate the nitrogenase iron molybdenum cofactor (FeMoco).[35] They found that the positively charged Fe site in MoS_2 could act as an effective center for absorbing N_2 by contributing electrons to the antibonding orbital of N_2, ultimately activating N_2 through the acceptance–donation process.

3.1.2. Nonmetal Doping

Due to the price concerns for the precious metals (such as Ir, Pt, and Ru), the other doping strategy using cheap nonmetal atoms is also widely developed. Delightfully, the resulting catalytic materials also displayed satisfactory NRR performance. The most widely employed nonmetal-atom dopant is boron (B) atom. In 2018, Hering-Junghans reported that hypovalent B species with the coexistence of lone-pair electrons and empty orbitals are similar to transition metals.[36] When doped into carbon materials, the B atoms could be positively charged and provided empty orbitals. Based on the Lewis theory that N_2 is a weak Lewis base, fabricating Lewis acid sites (empty orbitals of B) is considered to be a favorable strategy to realize the N_2

**ADVANCED
SCIENCE NEWS**
www.advancedsciencenews.com
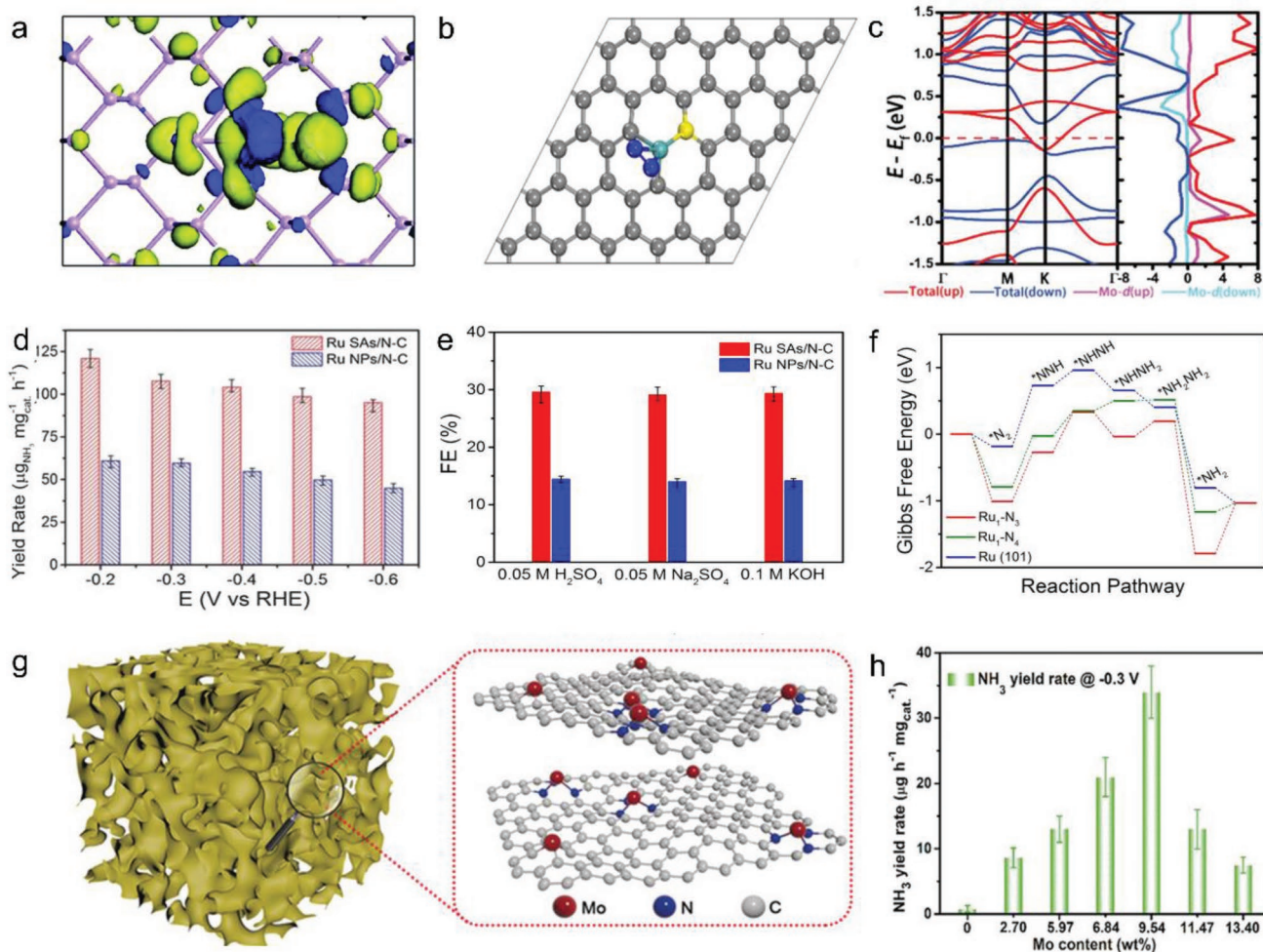
**ADVANCED
ENERGY
MATERIALS**
www.advenergymat.de

Figure 2. a) Top view of spin density distribution. Blue and yellow isosurfaces represent positive and negative spin densities. Reproduced with permission.[27] Copyright 2018, Royal Society of Chemistry. b) Top view of $Mo_1–N_1C_2$ with N_2 adsorbed by side-on configuration. c) Band structure and density of states of $Mo_1–N_1C_2$ which show metallicity. The red and blue lines in band structure mean the majority spin and minority spin components, respectively. The Fermi level is set to zero. Reproduced with permission.[28] Copyright 2018, American Chemical Society. d) NH_3 yield of Ru SAs/N–C and Ru NPs/N–C at various potentials. e) The FE of Ru SAs/N–C in three types of electrolyte. f) The changes of Gibbs free energy of $Ru_1–N_3$, $Ru_1–N_4$, and Ru (101) through an alternating pathway. Reproduced with permission.[31] Copyright 2018, Wiley-VCH. g) The structure of Mo@NPC including its atomic model. h) NH_3 yield of Mo@NPC complexes with various Mo content. Reproduced with permission.[33] Copyright 2019, Wiley-VCH.

adsorption. Besides, the lone-pair electrons of B atom could fill in the antibonding orbitals and activating N≡N triple bond.

In 2018, Zheng's group simulated the molecular orbitals of B-doped graphene.[37] By detailed analysis, the B dopant introduced inhomogeneity for graphene and exhibited positively charged (**Figure 3**a), which is favorable for N_2 adsorption. Among the four configurations (B_4C, BC_3, BC_2O, and BCO_2), BC_3 was found to be advantageous for the NRR. Furthermore, the experimental results demonstrated that the graphene with 6.2% B-doping attained a high FE value of 10.8% and a NH_3 yield of 9.8 µg h^{-1} cm^{-2} (Figure 3b). To overcome the toxic effect of the edge sites in the pristine boron nitride (BN) caused by the sluggish ammonia desorption, Du and co-workers constructed the single B-atom-modified BN edge.[38] The novel structure with a boron-atom-modified edge had a relatively low overpotential of 0.13 V, and the generated NH_3 could be rapidly removed with a small energy barrier of 0.35 eV. At the

same time, Ji et al. reported the possibility of B-doped C_2N layers with three kinds of dopant configurations (Figure 3c) as NRR electrocatalysts due to three advantages: i) the end-on configuration of B_N (the N atom is replaced by the B atom) and B_{int} (the B atom interstitially doped in the C_2N layer) has short and strong B−N bond, elongating the N≡N bond; ii) the B_{int} atom provides 0.1 µB magnetic moments to the adsorbed N_2, meaning a stronger adsorption; iii) the B_{int} reduces the bandgap of C_2N, promoting intrastratal electron transfer.[39] Cao et al. further analyzed the NRR properties of single and double B-atoms-doped C_2N monolayer ($B@C_2N$, $B_2@C_2N$) on the theory level.[40] By comparing the lattice energies, the $B_2@C_2N$ model was found to be more thermodynamically stable, and the N_2 adsorbed on biatoms' doping sites could be much easier to acquire electrons, supported by the plot of electronic localized function (ELF) in Figure 3d. As a consequence, the $B_2@C_2N$ had a more significantly lower potential for NRR (ΔG_{max} of
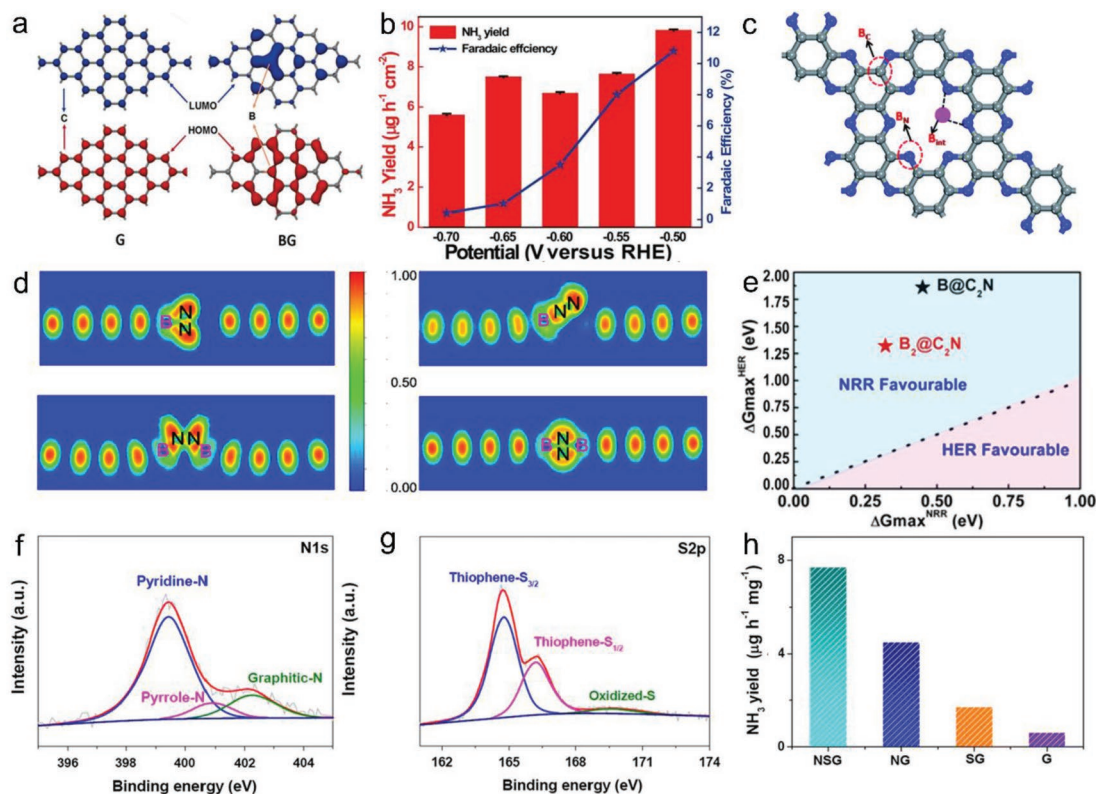
Figure 3. a) The lowest unoccupied molecular orbital (blue) and highest occupied molecular orbital (red) of undoped graphene and B-doped graphene. b) The NRR performance of the B-doped graphene. Reproduced with permission.[37] Copyright 2018, Elsevier. c) Three different configurations of B doped in graphene including B_N, B_C, and B_{int}. Reproduced with permission[39] Copyright 2019, Royal Society of Chemistry. d) The electronic localized function (ELF) plot of N_2 on $B@C_2N$ and $B_2@C_2N$. The red, green, and blue regions indicate the high local electron distribution, electronic-gas-like pair probability, and high electronic delocalized distribution. e) The energy request for HER and NRR, indicating the tendency between these two reactions. Reproduced with permission.[40] Copyright 2019, IOP Publishing. XPS spectra of NS@G including f) N 1s and g) S 2p spectra. h) The NH_3 yield of NS@G, N@G, S@G, and undoped G. Reproduced with permission.[50] Copyright 2019, Springer Nature.

0.35 eV) than $B@C_2N$ (0.45 eV), and exhibited an extremely low overpotential of −0.19 V. As shown in Figure 3e, they further observed the propensity of the two catalysts for NRR and HER, where the $B_2@C_2N$ is more inclined to catalyze NRR. At present, it should be noted that the B-doped C_2N for NRR only stays at the level of theoretical prediction.

Due to the easy synthesis, the N-doping materials were widely reported. Since the N element has higher electronegativity than carbon, the doping of N is considered to regulate the electron density of C with more positive charges, which is beneficial to the adsorption of N_2. Therefore, the N-doped carbons are often used as NRR catalysts. Notably, lots of N-doped materials are derived from ZIF precursor, which is a type of porous materials with different topological structure and high porosity. The N species are usually divided into three types: i) pyridinic N (located in a hexa-heterocycles ring), ii) pyrrolic N (located in a penta-heterocycles ring), and iii) graphitic N (in-plane replace the carbon plane).[41]

In 2018, Wu's group reported a ZIF-derived NPC as an NRR electrocatalyst, attaining an FE of 10.2% and a NH_3 yield of 3.4×10^{-6} mol cm^{-2} h^{-1} (−0.3 V).[42] They found that the graphitized N was not the adsorption site of N_2, but could regulate the electronic structure and affect the adsorption energy of other reaction sites. The only possible active sites are triatomic

nitrogen coordination configurations containing a protonated pyridinic N and an adjacent vacancy. Zhao and co-workers also reported an NPC catalyst derived from ZIF-8, demonstrating that pyridinic N and pyrrolic N are active sites for ammonia synthesis, where the pyridinic and pyrrolic N mediated the electronic structure of carbon nanomaterials and caused the defect formation and charge polarization.[43] As a result, the optimized NPC achieved a NH_3 yield of 1.40 mmol g^{-1} h^{-1} at −0.9 V.

Owing to the advantages of the N dopant for the electrocatalytic performance of the TM@C, some groups constructed the models of synergetically doping TM and N atoms into carbon matrix (TM/N@C). For instance, Du's group predicted the synergistic effect of different configurations between W and N dopants on W/N@graphyne.[44] They found that with increasing the coordination number of central W atoms, the NRR gradually deviated from thermoneutrality and the N_2 adsorption was weakened. Therefore, the W−N configuration was predicted as the most suitable configuration with an energy of about 0.31 eV for hydrogenation activation and an overpotential of 0.29 V for NRR. Recently, Qiao and co-workers established the models with various TMs and N doping into carbon-based matrix (g-C_3N_4), further confirming the synergy effect.[45] Then, Yin et al. synthesized atomically dispersed Co and N on carbon as NRR catalysts.[46] They found that the N atom

ADVANCED
SCIENCE NEWS

www.advancedsciencenews.com

ADVANCED
ENERGY
MATERIALS

www.advenergymat.de

at Co-N_x configuration showed similar action as the pyridinic N, and it also participated in the formation of the active sites along with the Co dopants. As a consequence, the Co–N_x site-enriched catalyst achieved an FE of 21.79% and a NH_3 yield of 1.57×10^{-10} mol s^{-1} cm^{-2} (−0.9 V vs Ag@AgCl).

Due to the weaker coordination ability, the chalcogen atoms (such as O, S, and Se) can regulate original atoms with more dangling bonds. Therefore, the chalcogen atom doping was also an effective strategy to engineer the NRR activities. In 2019, Sun and co-workers prepared a S-doped carbon nanosphere (S@CNS) with a NH_3 yield of 19.07 µg h^{-1} mg_{cat}^{-1} and an FE of 7.47% at −0.7 V, nearly fourfold enhancement when compared with that of the undoped one (3.70 µg h^{-1} mg_{cat}^{-1}; 1.45%).[47] Recently, they further introduced oxygen (O) into porous carbon nanosheet.[48] The resulted catalysts could achieve a high FE of 10.3% with the NH_3 yield of 18.03 µg h^{-1} mg_{cat}^{-1}. Simultaneously a higher NH_3 yield rate of 25.12 µg h^{-1} mg_{cat}^{-1} could be realized by the O-doped hollow carbon microtubes.[49]

Besides the above cases using only one nonmetal element for doping, using bi-nonmetal elements for multivariate co-doping has also been developed currently due to the more flexible configurations, which is believed to activate the adjacent C atoms to be the active sites when introduced into carbon-based matrices. In 2019, Liu and co-workers first studied N/S co-doped graphene (NS@G) for electrocatalytic NRR.[50] From DFT calculation results, the presence of pyridine-N, pyrrole-N, and thiophene-S (Figure 3f,g) could induce positive charges on adjacent C atoms, which could enhance N_2 adsorption, elongate N−N bond, and accelerate the electron transfer. The as-prepared NS@G achieved a moderate FE of 5.8% and a NH_3 yield of 7.7 µg h^{-1} mg_{cat}^{-1} (−0.6 V) as well as a satisfied 24 h stability, exhibiting an electrocatalytic activity superior to non-co-doped graphene (Figure 3h).

3.2. Atom Vacancy

The vacancy engineering by introducing anion or cation vacancies can increase the ability to capture electrons, adjust the band structure, and change the reaction pathway. The introductions of various types of vacancies are quite different toward NRR. In this perspective, we present recent theoretical and experimental progresses on vacancy engineering for NRR catalysts.

3.2.1. Anion Vacancy

Anion vacancy engineering, which mainly includes introducing oxygen vacancies (V_{Os}) and nitrogen vacancies (V_{Ns}), is predicted and proven to play an active role for NRR in many recent works.[15,51–56,58–67] Based on the early work's foreshadowing, the internal mechanism of anion vacancies for enhanced NRR is gradually revealed.

The V_{Os} can effectively capture electrons in a metastable state and inject them into the antibonds of N_2, so as to realize the electron acceptance–donation process. The V_{Os} have been widely proved to effectively activate the surface of the catalysts particularly the metal oxides. In the past few years, CeO_2 has been regarded as a promising matrix in catalytic applications due to

the compatible Ce^{3+}/Ce^{4+} redox couple. Hence, various composites based on CeO_2 have been developed with V_{Os} for NRR. Yu and co-workers reported an amorphous $Bi_4V_2O_{11}$/CeO_2 hybrid (BVC-A) structure with abundant defects.[51] A large number of V_{Os} in the as-prepared catalyst brought the back-donation bonds for electrons, leading to the excellent NRR performance (NH_3 yield: 23.21 µg h^{-1} mg_{cat}^{-1}; FE: 10.16%). To induce more V_{Os}, Zhang and co-workers reported a room-temperature approach to get core–shell Au@CeO_2 NRR catalyst.[52] With the introduction of gold core, the concentration of V_{Os} increased significantly proved by electron paramagnetic resonance (EPR) results, which boosted the NRR activity with a NH_3 yield of 28.2 µg h^{-1} cm^{-2} and an FE of 9.50% at −0.4 V. Cr was also introduced into CeO_2 to generate V_{Os} and acted as one of the active substrates.[53] Theoretical simulation revealed that the Cr dopants could reduce the energy barriers on V_{Os} sites to 1.04 eV. As a consequence, the Cr-doped CeO_2 exhibited considerable increase in NRR performance (NH_3 yield: 16.82 µg h^{-1} mg_{cat}^{-1}; FE: 3.84% at −0.7 V) than pure CeO_2 (NH_3 yield: ≈4 µg h^{-1} mg_{cat}^{-1}; FE: almost zero). Inspired by the Cu-doped CeO_2 for CO_2 reduction, Zhao and co-workers confirmed this kind of structure is also active for NRR.[54] Through Cu doping, they succeeded in adjusting the V_{Os} concentration in the CeO_2. By precise adjustment, the catalyst exhibited a NH_3 yield of 5.3×10^{-10} mol s^{-1} cm^{-2} with an FE of 19.1% at −0.45 V in 0.1 M Na_2SO_4 electrolyte.

Apart from CeO_2, TiO_2 is also a promising matrix and has drawn much attention from researchers. A defective TiO_2 on Ti mesh (d-TiO_2/TM) was prepared by Yang et al. to catalyze the NRR.[55] The V_{Os}-enriched TiO_2 showed a NH_3 yield of 1.24×10^{-10} mol s^{-1} cm^{-2} and an FE of 9.17% at −0.15 V. Actually, the NRR activities of TiO_2 depend largely on the concentration of V_{Os}. Sun and co-workers studied the NRR activity of TiO_2 by modulating the concentration of surface V_{Os} (**Figure 4**a) achieved by controlling annealing temperature.[56] Based on DFT studies, they found the surface V_{Os} in anatase TiO_2 can increase N_2 adsorption and activate the first protonation step. The V_{Os}-rich anatase TiO_2 achieved a NH_3 yield of about 3.0 µg h^{-1} mg_{cat}^{-1} and an FE of 6.5% at −0.12 V. MXene, a new family of 2D materials with hydrophilic surface, has been used as defect-rich TiO_2 precursor and matrix. Xu et al. prepared the V_{Os}-rich TiO_2/$Ti_3C_2T_x$ by one-step ethanol thermal treatment of the $Ti_3C_2T_x$.[57] On their discovery, the V_{Os} were considered to be the main active sites during the NH_3 evolution, and the interior $Ti_3C_2T_x$ nanosheets could enhance the electron transport and avoid the self-aggregation of the TiO_2 nanoparticles. NRR on TiO_2/$Ti_3C_2T_x$ through a typical distal pathway was achieved with comparatively small barriers of 0.4 eV (compared with 0.64 eV on $Ti_3C_2T_x$ and 0.54 eV on TiO_2), a high NH_3 yield of 32.17 µg h^{-1} mg_{cat}^{-1}, and an FE of 16.07% at −0.45 V in 0.1 M HCl.

As for other kinds of transition metal oxides, oxygen vacancy engineering is equally applicable. In order to suppress the competitive effect of HER, Zhang and co-workers artificially induced V_{Os} into α-Fe_2O_3 nanostructure, which is inert for hydrogen adsorption and sluggish for HER, thus promoting the electrocatalytic NRR performance, leading to an FE of 6.04% and a NH_3 yield of 0.46 µg h^{-1} cm^{-2} at −0.9 V versus Ag/AgCl.[58] Qu's group synthesized deficiency-abundant MoO_2 by chemical vapor deposition (CVD), exhibiting a novel distal/alternating hybrid
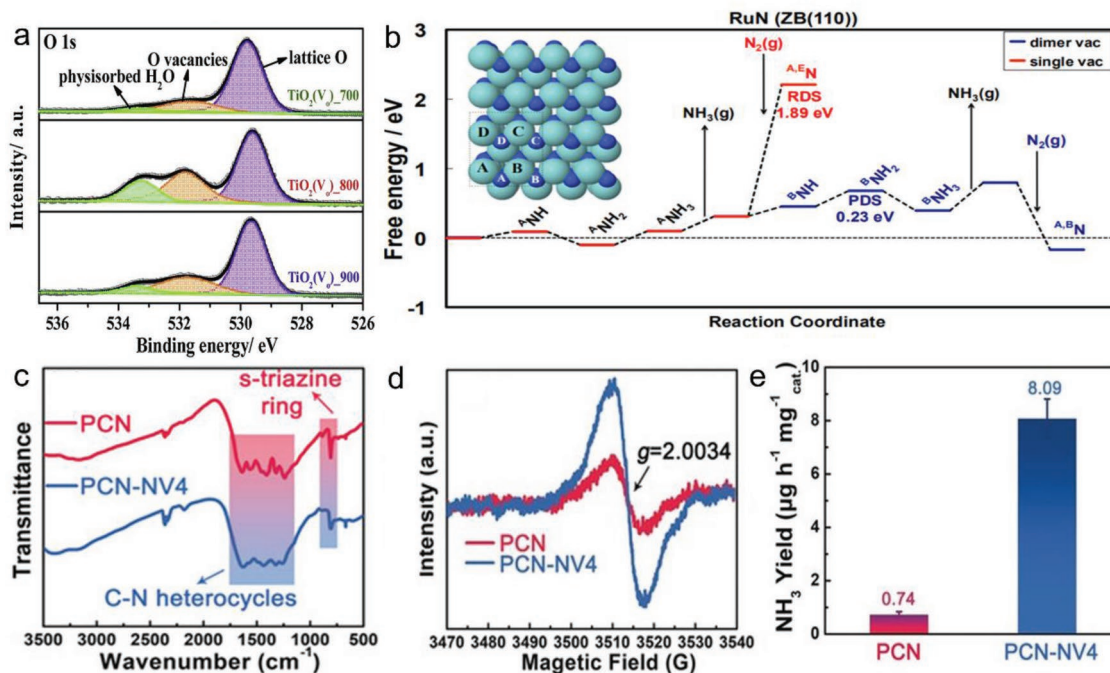
ADVANCED
SCIENCE NEWS
www.advancedsciencenews.com

ADVANCED
ENERGY
MATERIALS
www.advenergymat.de

Figure 4. a) The O 1s XPS spectra of TiO_2 with different annealing temperatures. Reproduced with permission.[56] Copyright 2019, Elsevier. b) Free energy diagram of mono- and dimer-vacancy MvK pathways on RuN. Reproduced with permission.[60] Copyright 2017, American Chemical Society. c) FTIR spectra, d) EPR spectra, and e) NH_3 yield of PCN and PCN with V_{Ns}. Reproduced with permission.[64] Copyright 2018, Wiley-VCH.

path for the reduction of nitrogen that has not been reported before.[59] In their results, a very low overpotential of around 0.15 V was achieved with a NH_3 yield of 12.20 μg h^{-1} mg$_{cat}$$^{-1}$ and an FE of 8.2%. They also confirmed that only an appropriate amount of V_{Os} could donate proper amount of electron on Mo^{3+} ions to enhance the catalytic NRR activity.

In recent years, metal nitrides (MNs) are identified to hold great potential for NRR due to the possibility of Mars–van Krevelen (MvK) reaction mechanism. Unlike the general reaction pathway, in MvK reaction mechanism, the reactive lattice-N can be directly protonated to ammonia and leaves V_{Ns} on the catalyst surface. Then the dissolved N_2 subsequently replenishes the V_{Ns} to complete the catalytic cycle. It has been theoretically predicted that the V_{Ns} in transition metal nitrides could induce and accelerate the MvK reaction process.

In 2016, Skúlason's group carried out detailed theoretical calculations on several MNs including VN, ZrN, NbN, and CrN. They found the filling rate of vacancy was higher than its formation on these reasonable catalysts.[15] By calculating the free energy of different atoms adsorbing on the surface vacancy, N is found to be the most inclined to replenish the surface vacancy among N, O, OH, and H atoms due to the negative value of $\Delta G_{(*2N-*X)}$, demonstrating the high selectivity for N atoms. The effect of adsorbed oxygen on the catalyst surface was further considered, and they pointed out that electrochemical removal of surface oxygen is required before NRR. In 2017, Abghoui and Skúlason put forward a new standpoint that on the (110) orientation of the zinc-blende structured MNs, MvK pathway was more appropriate on the dimer N-vacancies.[60] By computing the ΔG variation tendency and the overpotentials of mono- and dimer-vacancy MvK pathways in Figure 4b, they

found that the dimer-vacancy MvK pathway had lower energy barriers and lower overpotentials among RuN, CrN, and WN, revealing that the MvK reaction mechanism is a more ideal pathway for these MNs. Experimentally, Catlow's group further unveiled the MvK mechanism of the NRR process on Co_3Mo_3N by the isotope labeling method in 2018.[61] Sun's group also found the superiority of the MvK mechanism for MNs like Mo_2N nanorods (NRs).[62] As compared to the MoO_2, the Mo_2N nanorod exhibited a dramatically reduced free energy barrier (ΔG_{H*}) of 0.58 eV and achieved a significantly enhanced yield (78.4 μg h^{-1} mg$_{cat}$$^{-1}$) and FE (4.5%) at −0.3 V. They also obtained a NH_3 yield of 3.01×10^{-10} mol s^{-1} cm^{-2} with an FE of 1.15% by employing the MoN nanosheets array as the catalyst.[63]

In addition to causing the MvK mechanism in the metal nitrides, the presence of V_{Ns} in metal-free matrix can also contribute to the tailored electronic structure and N_2 adsorption. For example, Yu's group artificially introduced V_{Ns} into layered polymeric carbon nitride (PCN) to make it as an NRR catalyst.[64] With the re-calcination in an atmosphere of argon, the number of s-triazine rings was decreased and the π-electron delocalization was increased from the Fourier-transform infrared (FTIR) (Figure 4c). In addition, the stronger EPR obviously revealed the defect-rich characteristics (Figure 4d). As a result, the N_2 adsorption was strengthened at the V_{Ns} sites, which can be further confirmed by the auxiliary DFT calculation. When compared with the pristine PNC, the V_{Ns}-rich PCN showed a tenfold increase in NH_3 yield of 8.09 μg h^{-1} mg$_{cat}$$^{-1}$ (Figure 4e), clearly demonstrating the merits of V_{Ns} for improving the NRR activities.

In addition to the O and N vacancies, S and C vacancies could regulate the magnetic moment and the surface affinity

of the catalysts, which are favorable to NRR. In 2018, Garzon et al. predicted the C vacancies on the (111) plane of cubic MoC could mitigate the accumulation of H-adatoms and HER, and hence advantageously increase the surface affinity of the cubic MoC(111) for both nitrogen molecules and N-adatoms.[66] Huang's group demonstrated that the single-C vacancies in Fe-embedded graphene could adjust the magnetic moment of Fe sites through DFT calculations and thermodynamic analysis.[65] They emphasized the role of Fe magnetism on NRR with an advantageous adsorption process. In 2019, MacFarlane's group fabricated Ru nanoparticles on S-vacancies-rich MoS_2 as a highly selective NRR electrocatalyst with a high FE of 17.6% and a NH_3 yield of 1.14×10^{-10} mol s^{-1} cm^{-2} at 50 °C.[67] In their report, the S vacancies in the MoS_2 matrix can act as the H-adsorption sites and provide H atoms for the synthesis of ammonia.

3.2.2. Cation Vacancy

The strategy of introducing anion vacancies is intensely sought after at this moment; however, the investigation of cation vacancies has attracted relatively little attention, and related research remains at an early stage. Enlightened by the cation vacancy–engineered catalysts for water splitting, it is reasonable to anticipate that the cation vacancies may show much potential to facilitate the NRR.[68,69]

Given that the semimetal bismuth (Bi) has a weak binding with the adsorbed H atom, exploiting Bi to suppress HER is brimming with possibilities to design efficient catalysts for NRR. In a bid to address the problem that the stable valence electron structure of Bi is detrimental to the adsorption and activation of N_2, Jiang and co-workers introduced defects into Bi to change its electronic structure.[70] They fabricated defect-rich Bi (110) nanoplates through a low-temperature plasma bombardment technology on Bi_2O_3 nanoplates. DFT calculation proved that the active barrier of the as-prepared nanoplate is much lower than that of the ideal plate, which is consistent with the observation from the experiments that the as-prepared Bi nanoplate with Bi vacancies exhibits an enhanced FE of 11.68%. Wen and co-workers proposed a N-doped carbon-coated γ-Fe_2O_3 nanoparticles supported on carbon fabric (γ-Fe_2O_3-NC/CF) for NRR.[71] A portion of the Fe cations were found to escape from the γ-Fe_2O_3 atomic lattice during the activation process in HCl electrolyte, thus forming cation vacancies conducive to the NRR. A high FE of 12.28% and a NH_3 yield of 11.7×10^{-10} mol s^{-1} cm^{-2} were achieved, and the Fe vacancy was considered as one of the contributors for the high electrocatalytic performance.

4. Surface Orientation and Amorphization

NRR as a representative surface reaction, the different surface configurations of the electrocatalysts become the decisive key. According to the surface orientation and crystallization of the crystals, the effect of the crystal orientation, atomic step, and amorphization of the catalysts on NRR are reviewed in this section.

4.1. Crystal Orientation

In the traditional Haber–Bosch ammonia synthesis process, the catalytic performance of the most commonly used iron-based catalysts is closely related to the surface orientation. Different crystal faces of iron for NRR are often compared, and the adsorption strength of N atom on Fe (100) surface is stronger than that on Fe (110) and (111) surfaces.[72] The reaction mechanism and kinetics on the specific oriented surfaces, such as Fe (111) and (211), have also been studied intensively.[73] In addition, (110) crystal plane of Mo has been evidenced theoretically for competitive NRR, because the adsorption energy for nitrogen is −1.1 eV, much lower than that for hydrogen (only −0.7 eV).[74] Therefore, nitrogen can be effectively combined on the surface of Mo for the reduction process in NRR without inhibition by the competitive HER reaction. Experimentally, Wang's group verified the fascinating catalytic NRR activity of the (110)-oriented Mo.[75] In their results, the catalytic activity of the catalyst improved with the increase of (110) orientation while decreased with the increase of (211) orientation, demonstrating the superior (110) surface of Mo tends to promote NRR, while the (211) surface of Mo is more favorable for H adsorption. The as-optimized Mo catalyst showed an FE of 0.72% at −0.29 V, which was almost 4.5 times higher than that of commercial Mo foil.

In addition, the possibility of chemical ammonia synthesis in water electrolytes was further studied by Abghoui and Skúlason from the (111) facets of TiN, VN, CrN, MnN, ZrN, NbN, MoN, HfN, WN, and ReN.[76] Through the theoretical analysis, it was found that the crystal plane of the nitrides owns strong selectivity for the electroreduction of nitrogen. This research further confirms that electrocatalysis is a surface-sensitive process, inspiring successors to focus more on the regulation of the crystal orientation in the catalyst design.

4.2. Stepped Facet

Stepped sites are generally considered to be a kind of high-energy surface defects that can reduce the energy barrier of the catalytic reaction. Previous theoretical studies have revealed that the stepped facet is a better active center on the catalyst for NRR.[23,77,78] In general, the number of stepped sites is inversely proportional to the activation energy of N_2 dissociation. Theoretically, the binding of the intermediate product to the active center on the stepped sites was stronger than that on the flat terrace, which greatly optimized the activity of the metal-based catalyst.

The effect of the stepped facets on the metal catalyst was analyzed by Nakai and co-workers.[79] They discussed the synthesis of NH_3 on Ru, Os, and Rh nanoparticles by the plane-wave DFT method. As for the nanoparticles with a diameter of 2.5–5 nm, Rh exhibits the largest surface energy among the three metals, which can be ascribed to the formation of stepped facets between (111) and (100) faces. The stepped sites provide a stronger bond to the nitrogen, inducing a higher NRR rate than the other surfaces.

Tetrahexahedral gold nanorods with high-index {730} planes composed of (210) and (310) subplanes were also explored
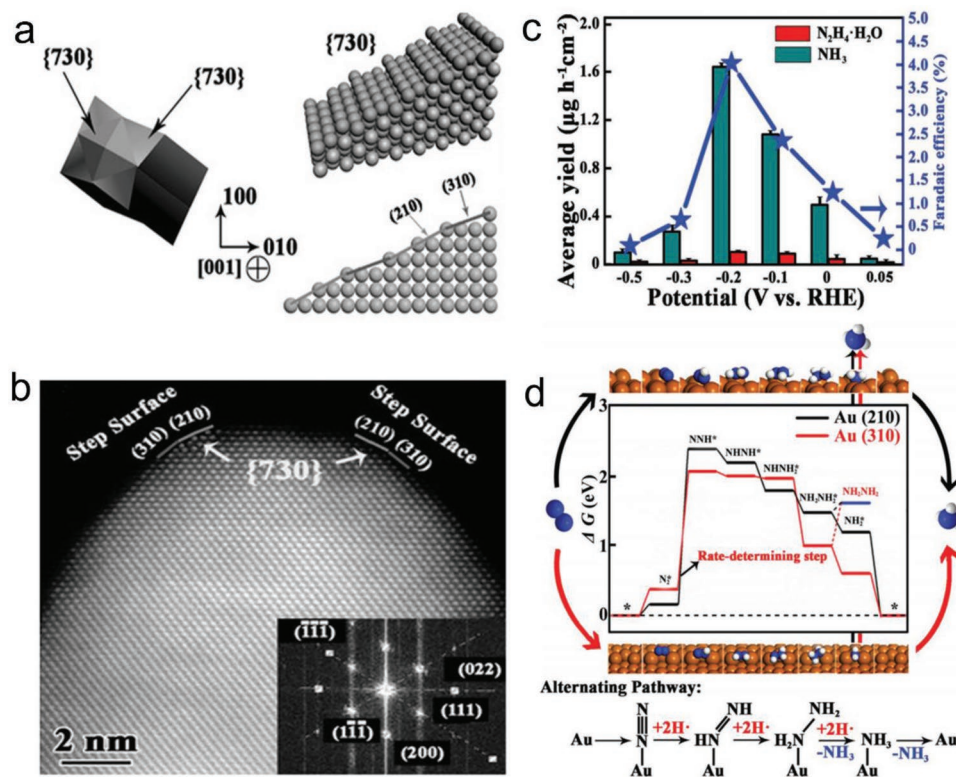
ADVANCED
SCIENCE NEWS
www.advancedsciencenews.com

ADVANCED
ENERGY
MATERIALS
www.advenergymat.de

Figure 5. a) Atomic structure of tetrahexahedral (THH) Au NR. The {730} facet is a multistep surface composed of (210) and (310) subplanes. b) Spherical aberration corrected transmission electron microscope image of THH Au NR, the inset is the fast Fourier-transform pattern of the indicated region. c) NH_3 yield, N_2H_4 formation, and the FE of THH Au NR. d) Free energy diagram and alternating hydriding pathway on Au (210) and Au (310). Reproduced with permission.[80] Copyright 2017, Wiley-VCH.

experimentally for NRR (**Figure 5**a,b).[80] The rich exposed (310) and (210) subplanes exposed on the catalyst can provide a large number of catalytic active sites to capture and dissociate N_2, thus attaining an unexpected high NH_3 yield of 1.648 µg h^{-1} cm^{-2} at −0.2 V under ambient conditions (Figure 5c). In this report, an alternating hydrogenation mechanism was proposed as shown in Figure 5d. Briefly, weak adsorption of N_2 on the stepped facets can be formed due to the unsaturated coordination as N_2 and H_2O approaching the surface of the Au NRs. Then, the activated H produced by water electrolysis forms a relatively stable N—H bond with the N atom, which promotes the cleavage of the N≡N triple bond. Finally, H atoms from the electrolyte as well as electrons on the electrode surface are successively added to N atom for N_2 hydrogenation.

4.3. Amorphization

Amorphous material has no long-range order in the internal structure when compared with the crystalline counterpart, which makes it one of the ideal candidate catalysts for various electrochemical reactions due to its unique properties such as abundant surface, rich bulk defects, as well as extraordinary localized electronic structure. It has been confirmed that the crystallinity, like other factors such as defects and surface step, is responsible for the electrocatalytic activity of the catalyst.[81] A large number of unsaturated coordination sites resulted from dangling bonds,

as well as more introduced defects, endow amorphous material with significantly enhanced activity. Some research efforts have been devoted to revealing the enhancement of intrinsic activity by amorphization.[81–83] It is generally accepted that amorphous bimetallic oxide is a relatively well-characterized catalyst for OER and ORR, which gave rise to a new discussion on the possible applications in other electrochemical catalytic reactions, especially the NRR, that are trapped in dynamic hysteresis and competitive reaction. The strategy of converting crystals into amorphous state shows promising prospects; however, further effort is required to shed light on the internal mechanism and development direction. In this section, amorphous metallic catalysts and nonmetallic catalysts developed for NRR in recent years are summarized. Through the further understanding of the NRR performance of amorphous catalysts, researchers may get some inspiration that can help the further improvement.

Taking the excellent catalytic activity and the high price of noble metals into account, a growing amount of research has been emphasized on how to enhance the inherent activity of the noble-metal-based catalysts, including the transition to amorphous materials. Considering the intriguing features including the unique 4f electrons, which play a significant role in electronic transfer, CeO_x has been employed not only for the formation of amorphous structures but also as an assistant for electron transport.[84] For instance, amorphous Au NPs anchored on CeO_x-RGO was fabricated by Yan's group through a facile coreduction method at room temperature, showing outstanding
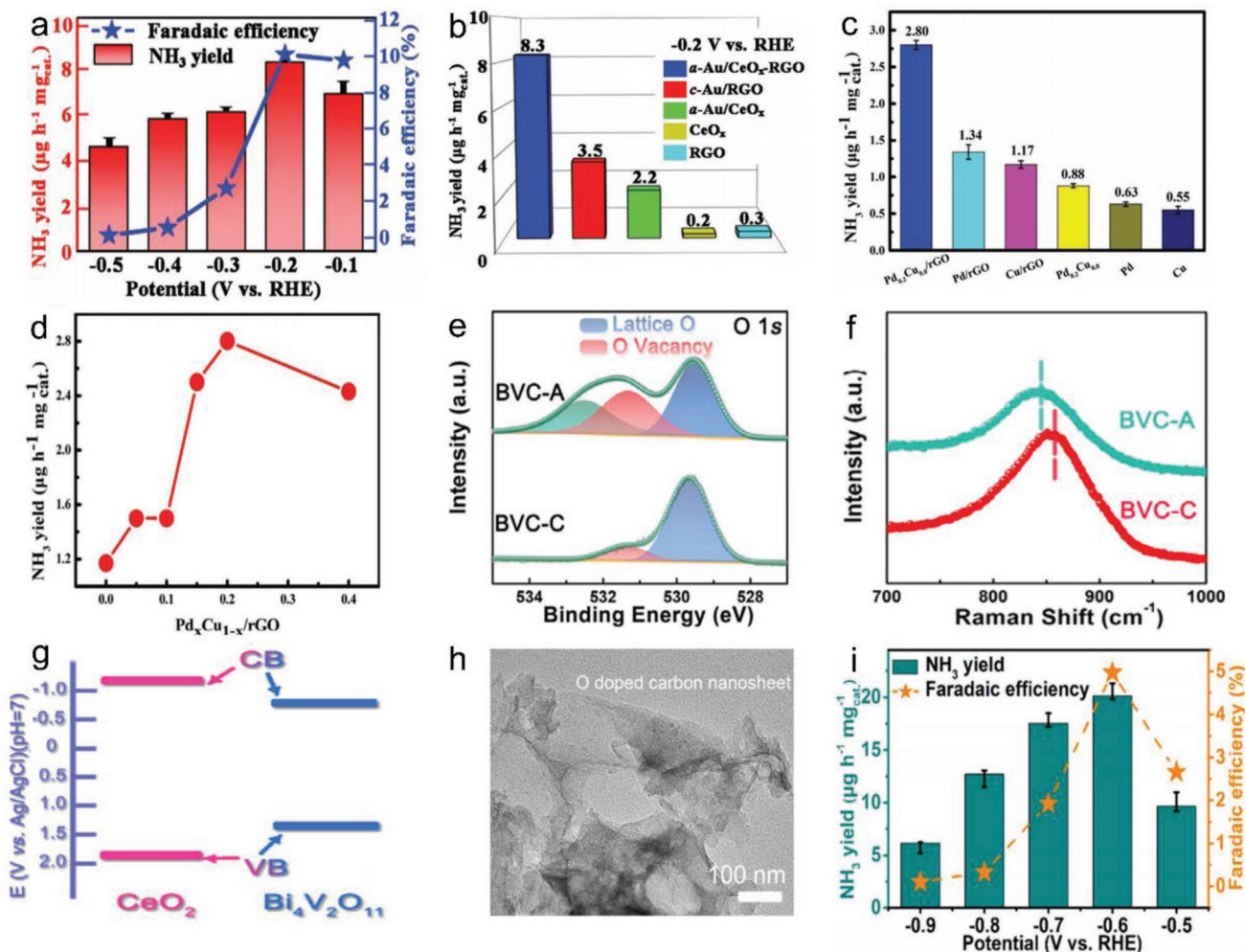
Figure 6. a) NH_3 yield and FE at different potentials of the a-Au/CeO$_x$-RGO catalyst. b) NH_3 yield of different catalysts at −0.2 V. Reproduced with permission.[85] Copyright 2017, Wiley-VCH. c) NH_3 yield of Pd–Cu bimetallic composite, monometallic counterparts, and single metal at ambient condition. d) NH_3 yield of Pd–Cu bimetallic composites with different atomic ratios at ambient condition. Reproduced with permission.[87] Copyright 2018, Wiley-VCH. e) O 1s XPS spectra of BVC-A and BVC-C. f) Raman spectra of BVC-A and BVC-C. g) Band alignment schematic diagram of Bi$_4$V$_2$O$_{11}$ and CeO$_2$. Reproduced with permission.[51] Copyright 2018, Wiley-VCH. h) Transmission electron microscopy (TEM) image of O–CN. i) The FE and NH_3 yield of as-obtained O-CN at various potentials. Reproduced with permission.[88] Copyright 2019, Wiley-VCH.

electrocatalytic NRR performance with an FE of 10.10% and a NH_3 yield of 8.3 µg h^{-1} mg$_{cat}^{-1}$ (**Figure 6**a).[85] The introduction of CeO$_x$ destroyed the long-range order of Au NPs, and the disorder of Au NPs can also be traced to the lattice strain effect due to the different oxidation states of Ce.[86] Therefore, it is reasonable to elucidate that the enhanced electrocatalytic activity could be credited to the much more unsaturated coordination sites of amorphous Au NPs with structural distortion. As compared to the other control samples, the amorphous catalyst performs not only better catalytic activity (Figure 6b), but also pretty good selectivity and stability. Giving that the as-prepared amorphous catalysts show low content of noble metals and can be prepared at room temperature, it is expected to exhibit better catalytic performance and provides practical guidance for subsequent development for other noble-metal-based materials.

Combining noble metals with transition metals, which would not only reduce the use of noble metals but also effectively improve the catalytic performance, is also a promising mean that

has been emphasized. Based on the previous studies focused on the amorphous monometallic catalyst, Yan and co-workers synthesized an amorphous Pd-Cu bimetallic composite for activating the NRR.[87] As shown in Figure 6c,d, the as-prepared Pd$_x$Cu$_{1−x}$ amorphous nanoclusters anchored on reduced graphene oxide (rGO) exhibited an improved catalytic activity for NRR when compared with monometallic counterparts, among which the Pd$_{0.2}$Cu$_{0.8}$/rGO composite showed the optimal performance and excellent selectivity. In addition to the synergistic electron effect of bimetals, the high surface area of the amorphous catalyst and abundant dangling bonds served as active sites also contribute to the improvement of the activity. This result effectively alleviates the dependence on noble metals, while ensuring enough catalytic activity, which shows a tremendous guiding role for future studies about amorphous bimetallic or even trimetallic catalysts.

As mentioned above, Yu's group obtained amorphous-phased BVC-A with high density of defective sites through electrospinning and subsequent calcination approach.[51] In

ADVANCED
SCIENCE NEWS
www.advancedsciencenews.com

ADVANCED
ENERGY
MATERIALS
www.advenergymat.de

their results, defective state of V^{4+} species was found, which possesses tremendous potential for the π back-donation process, giving rise to the cleavage of N≡N triple bond, breaking through the limitation of Bi^{5+} without d orbital. What is more, the increase of oxygen vacancies could be also detected as confirmed from O 1s X-ray photoelectron spectroscopy (XPS) spectra (Figure 6e) with a higher intensity, which is in favor of the nitrogen reduction process. The presence of defects in BVC-A was further evidenced by Raman spectroscopic investigation (Figure 6f). As shown in Figure 6g, a type I band alignment was established for the hybrid catalyst, thereby promoting the electron transfer at the interface. In addition, the BVC-A showed a vast number of dangling bonds standing out as an efficient part for offering active sites and reducing energy barrier. As a result, the as-obtained catalyst exhibited significantly improved NH_3 yield (23.21 µg h^{-1} mg_{cat}^{-1}) and high FE (10.16%) under ambient conditions at −0.2 V, pointing the way for subsequent development.

In addition to the amorphous metallic catalysts, nonmetallic carbon-based materials are also considered to be highly efficient and inexpensive catalysts for NRR. Sun's group successfully obtained amorphous oxygen-doped carbon nanosheet (Figure 6h) by carbonizing tannin in Ar gas at 900 °C.[88] The as-obtained amorphous catalyst attained high selectivity and stability with a yield of 20.15 µg h^{-1} mg_{cat}^{-1} and an FE of 4.97% at −0.6 V (Figure 6i), much better than a number of catalysts including some Fe- and Au-based catalysts. Very recently, the oxygen-doped hollow carbon microtube was first developed as a well-performed catalyst for NRR.[49] The amorphous carbon obtained from Kapok fibers achieved a high FE of 9.1% for NH_3 with a yield rate of 25.12 µg h^{-1} mg_{cat}^{-1} under ambient conditions, providing guidelines for burgeoning biomass-derived carbon-based catalysts.

5. Heterostructure Engineering

Taking full advantage of strengthened electron transfer and surface strain, heterostructure has been a useful strategy to construct strongly coupled interface with special targets in photoelectronic devices and energy conversion.[89–93] In the field of catalysis, compared to a single component, heterostructure plays an important role in improving the catalytic activity of materials due to the tuned electronic structure and the enhanced active sites at the interfaces between different components.[94,95] Liang and co-workers constructed PdO/Pd heterojunctions on carbon nanotubes for electrochemical ammonia synthesis.[95] The interaction between the metal–metal oxide interfaces does provide abundant stable active sites for the NRR activation, which significantly inhibits the HER at the same time. The results suggest that the Pd phase at the interface preferentially adsorbs N_2 molecule to form Pd−N_2 bonds, and the PdO forms a stable α-PdH phase capable of activating the N_2 molecule by proton transfer, thus reducing the overpotential of the NRR (**Figure 7**a). The relationship of irradiation time and reduction degree was further explored, and a moderate reduction degree was found to be beneficial to NRR (Figure 7b). Xie and co-workers proposed a strong-coupled CoS_2/NS-G (N- and S-doped reduced graphene) catalyst, with a high NH_3

yield rate of 25.0 µg h^{-1} mg_{cat}^{-1} at −0.2 V and an FE of 25.9% at −0.05 V.[96] At the interface between CoS_2 nanoparticles and graphene sheet, strong bridging bonds was successfully formed, which resulted in an accelerated electron transfer, demonstrating the importance of interfacial engineering for heterostructure system. It should be highlighted that this interfacial engineering strategy is not specific to a single material, but a general approach. By changing the raw materials, other efficient heterostructured catalysts with strong-coupled interface can be obtained.

As one of the heterogeneous structures, the core–shell structure has been designed largely and shows a widespread application in catalysis, energy storage, and biology due to its immense specific surface area, adjustable size, core–shell interface, and other unique physical and chemical properties. The core–shell structure has also been applied in electrocatalytic nitrogen fixation currently on account of some structural advantages. First, "shell" acts as a protective layer to protect the core components from corrosion or dissolution when is composed of stable-state phases.[97–99] For example, Yang et al. modified the gold core with metal-organic framework (MOF)-8 shell, which not only wrapped the gold core as a protective layer, but also regulated the diffusion layer near the surface of the gold core to promote the nitrogen fixation reaction.[98] Meanwhile, Peng et al. found that the carbon layer in Fe_3C@C heterostructure played a similar role in preventing the Fe_3C core from being corroded during the catalytic process.[99] Second, supernumerary active sites are introduced at the interface due to the tight bond between "core" and "shell;" meanwhile, the so-called "synergistic effect" or "strong coupling effect" from the core–shell structure may optimize the NRR activity as a contrast with that of each component.[100–102] For instance, Zhang et al. found that the synergistic effect between SeO ligand and Te nanorod can be ascribed to the formation of the Te–Sn–O configuration at the interface. They further verified that the exposure of lone pair electrons in this configuration could maximize the orbital overlap with N_2 for optimal N–N bond activation.[100] Third, the contact area between different components is expanded from two dimensions to three dimensions, optimizing the electron transfer between components and thus improving the NRR activity of the material. Luo's group synthesized a core–shell structure with Co_3O_4 derived from MOF and nitrogen-doped porous carbon (Figure 7c).[97] The study revealed that the nitrogen-doped porous carbon cage of the shell limited the diffusion of reaction intermediate generated during the rate-determining step of NRR, thereby increasing the concentration of the NRR reaction intermediate at the core–shell interface; the Co_3O_4 core captured a large number of electrons through its abundant oxygen vacancies, forming a rich electronic state to facilitate N_2 adsorption and the activation of N≡N triple bond by electrons entering the antibond orbit of the adsorbed N_2 molecule. The NH_3 yield of Co_3O_4@NC could reach 42.58 µg h^{-1} mg_{cat}^{-1}, much higher than that of the Co_3O_4 nanoparticles (11.87 µg h^{-1} mg_{cat}^{-1}) and nitrogen-doped porous carbon (15.28 µg h^{-1} mg_{cat}^{-1}) under the same conditions (Figure 7d). When the noble-metal-based core–shell structure is constructed, the high catalytic activity of the noble metal can be retained, and the preparation cost is also reduced, thus improving the utilization rate of the precious metal, which is of great significance for the practical
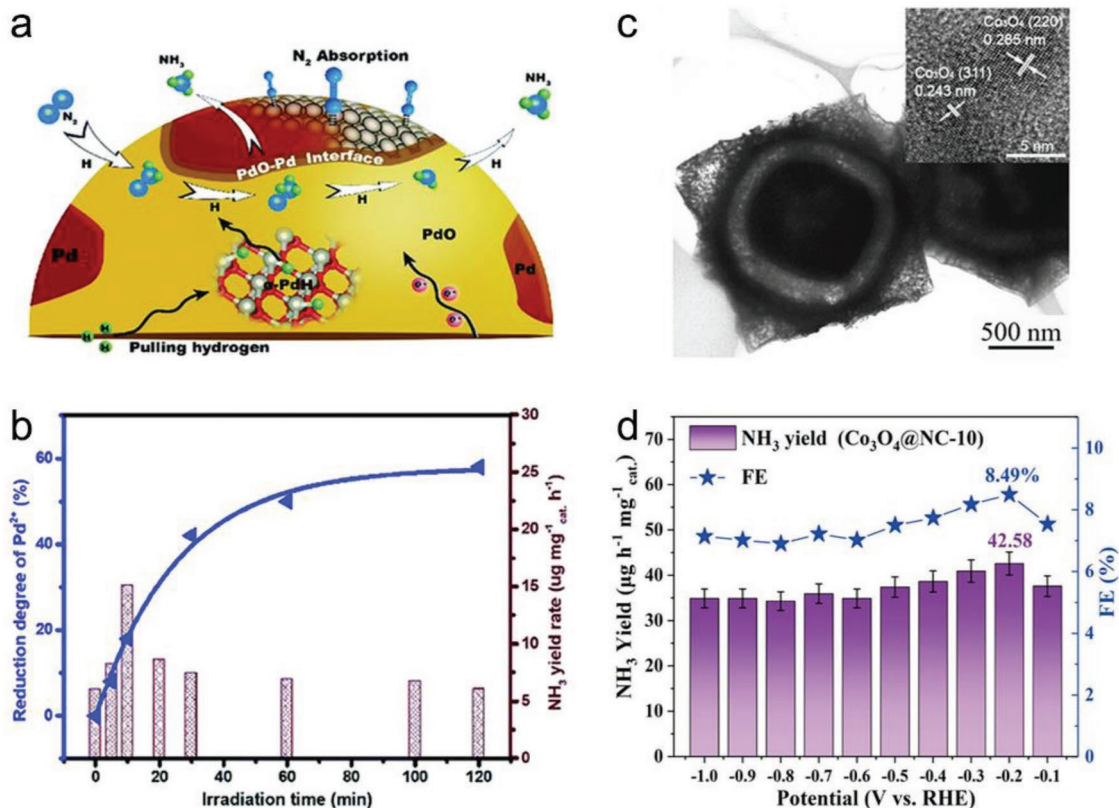
Figure 7. a) Alternative hydriding pathway on PdO/Pd heterostructures for NRR. b) The relationship of reductive degree and NH$_3$ yield of PdO/CNTs. Reproduced with permission.[95] Copyright 2019, Royal Society of Chemistry. c) TEM image of Co$_3$O$_4$@NC-10 with core–shell structure. Inset is the high-resolution TEM (HRTEM) image. d) NH$_3$ yield and FE of Co$_3$O$_4$@NC-10 at each given potential. Reproduced with permission.[97] Copyright 2019, American Chemical Society.

application of the precious metal in the NRR and can also be extended to the field of transition metals.[99,100]

At present, the design of heterostructures has become one of the common methods to improve the electrocatalytic nitrogen fixation performance. However, the application of core–shell structures is still less, meanwhile revealing a large space for exploration. For instance, the "synergistic effect" has not been conducted in an in-depth analysis, whose universality and relationship with phases, interfaces, materials, and defects are unclear. In previous studies, the "synergistic effect" was reflected in the higher NH$_3$ yields of the core–shell structure when compared with that of each component, and the analysis of the effect was mainly based on the correlation calculation about electron transfer, morphology, and structure, etc. The study about Co$_3$O$_4$@NC mentioned above has no direct observational evidence for the higher concentration of NRR reaction intermediates in the core–shell structure. In the follow-up study, the development of in situ observations of NRR reaction intermediates will help to explore and confirm the synergistic effect, allowing a single catalyst to better integrate the advantages of multiple materials.

6. Challenge and Outlook

Although the development period of electrocatalytic NRR is short, an integral theoretical–experimental framework in NRR

has been established with the synthesis and analysis of novel electrocatalysts. Significant progress on NRR electrocatalysts has been achieved with excellent electrochemical performance. However, in contrast with the Haber–Bosch, the as-reported NRR studies still have a long distance with industrial application. The further development of electrocatalytic NRR demands deeper mechanism analysis, boosted ammonia yield and FE, as well as more accurate and systematical measurement methods. Details are as follows:

1) *In Situ Characterization Techniques for NRR*: The NRR reaction pathway has been widely predicted and reported from the theoretical calculation perspective. Nonetheless, the elementary reactions and the formation of the intermediates have not been proven by more persuasive experiments. In this respect, the in situ characterization techniques (such as in situ FTIR, in situ Raman, and in situ attenuated total reflection surface-enhanced infrared absorption (ATR-SEIRA)) are powerful for detecting the transient states in the NRR process, through which the reaction pathway can be revealed directly.[103]

2) *The Lucubration of the Active Mechanism*: In recent 2 years, booming research of NRR has led to the discovery of a large number of NRR electrocatalysts. Some of them have excellent performance and the foreground for industrialization applications. However, research on the catalytic mechanism is still in its infancy. Therefore, the study should go deeper

ADVANCED
SCIENCE NEWS

www.advancedsciencenews.com

ADVANCED
ENERGY
MATERIALS

www.advenergymat.de

into the catalytic mechanism to provide guidance for the further design of NRR electrocatalysts.

3) *Integration of a Reaction System*: The H-type cells separated by Nafion proton exchange membrane (PEM) are widely used in current works. Because of the poor aqueous solubility, nitrogen needs to be continuously pumped into the electrolyte to keep a nitrogen-saturated environment. However, the bubbling nitrogen is unable to dissolve in the electrolytes, and it is also not conducive to industrial application. Therefore, more efficient nitrogen injection strategy (such as membrane penetration method) and electrolyte optimization (for example, using nonpolar solution or ionic liquid to improve nitrogen solubility) have a broad prospect.

4) *Accuracy of the Products' Detection*: In order to get reliable NH_3 yield and Faradic efficiency, the accuracy of the measurements for ammonia and hydrazine concentration is particularly important. At present, the indophenol blue and Nessler's reagent spectrophotometry are the most prevalent methods. For higher accuracy and reliability, the chromatography and ion-selective electrodes should be adopted. Moreover, ammonia pollution needs to be controlled and the interference of Nafion PEM should be excluded.

5) *High-Throughput Screening System for NRR Electrocatalysts*: Theoretical simulation has provided the predictions of NRR electrocatalyst candidates. However, until now, the experimental activity test is mainly achieved by manual testing, which seriously suspends the rapid development of NRR. Combining the automatic system and the programmatic testing, a high-throughput electrochemical test system can dramatically accelerate the confirmation period for theoretical predictions.

In summary, we have reviewed recent advances of atomic structure modification for electrochemical NRR, with emphasis on the catalytic mechanisms and effects. To achieve more rational catalysts, optimized reaction system, advanced characterization techniques, precise detection method, as well as high-throughput screening system are proposed to deepen the understanding of the active mechanism. Despite the daunting challenges ahead, the combination of theoretical calculations and experimental investigations is believed to provide a good platform to further promote the development of electrochemical ammonia synthesis. The specific atomic structure modification can not only benefit the NRR, but also be suitable for tuning similar cathodic reactions, including competitive catalysis and selective catalysis (e.g., CO_2 reduction reaction), paving the way for future energy issues.

Conflict of Interest

The authors declare no conflict of interest.

[1] P. Song, H. Wang, L. Kang, B. Ran, H. Song, R. Wang, *Chem. Commun.* **2019**, *55*, 687.
[2] C. Guo, J. Ran, A. Vasileff, S.-Z. Qiao, *Energy Environ. Sci.* **2018**, *11*, 45.
[3] C. J. Van der Ham, M. T. Koper, D. G. Hetterscheid, *Chem. Soc. Rev.* **2014**, *43*, 5183.
[4] H. Wu, H. N. Alshareef, T. Zhu, *InfoMat* **2019**, *1*, 417.
[5] X. Du, J. Huang, J. Zhang, Y. Yan, C. Wu, Y. Hu, C. Yan, T. Lei, W. Chen, C. Fan, J. Xiong, *Angew. Chem., Int. Ed.* **2019**, *58*, 4484.
[6] J. Huang, Y. Sun, Y. Zhang, G. Zou, C. Yan, S. Cong, T. Lei, X. Dai, J. Guo, R. Lu, *Adv. Mater.* **2018**, *30*, 1705045.
[7] J. Huang, Y. Sun, Y. Zhang, W. Wu, C. Wu, Y. Sun, R. Lu, G. Zou, Y. Li, J. Xiong, *J. Mater. Chem. A* **2018**, *6*, 9467.
[8] J. Huang, Y. Li, Y. Xia, J. Zhu, Q. Yi, H. Wang, J. Xiong, Y. Sun, G. Zou, *Nano Res.* **2017**, *10*, 1010.
[9] Y. Y. Birdja, E. Pérez-Gallent, M. C. Figueiredo, A. J. Göttle, F. Calle-Vallejo, M. T. Koper, *Nat. Energy* **2019**, *4*, 732.
[10] Z. Lu, G. Chen, S. Siahrostami, Z. Chen, K. Liu, J. Xie, L. Liao, T. Wu, D. Lin, Y. Liu, *Nat. Catal.* **2018**, *1*, 156.
[11] T. H. Rod, J. K. Nørskov, *J. Am. Chem. Soc.* **2000**, *122*, 12751.
[12] X. Li, X. Ren, X. Liu, J. Zhao, X. Sun, Y. Zhang, X. Kuang, T. Yan, Q. Wei, D. Wu, *J. Mater. Chem. A* **2019**, *7*, 2524.
[13] X. Zhang, R.-M. Kong, H. Du, L. Xia, F. Qu, *Chem. Commun.* **2018**, *54*, 5323.
[14] R. Zhang, Y. Zhang, X. Ren, G. Cui, A. M. Asiri, B. Zheng, X. Sun, *ACS Sustainable Chem. Eng.* **2018**, *6*, 9545.
[15] Y. Abghoui, A. L. Garden, J. G. Howalt, T. Vegge, E. Skúlason, *ACS Catal.* **2016**, *6*, 635.
[16] W. Qiu, X.-Y. Xie, J. Qiu, W.-H. Fang, R. Liang, X. Ren, X. Ji, G. Cui, A. M. Asiri, G. Cui, B. Tang, X. Sun, *Nat. Commun.* **2018**, *9*, 3485.
[17] Y.-C. Hao, Y. Guo, L.-W. Chen, M. Shu, X.-Y. Wang, T.-A. Bu, W.-Y. Gao, N. Zhang, X. Su, X. Feng, J.-W. Zhou, B. Wang, C.-W. Hu, A.-X. Yin, R. Si, Y.-W. Zhang, C.-H. Yan, *Nat. Catal.* **2019**, *2*, 448.
[18] L. Li, C. Tang, B. Xia, H. Jin, Y. Zheng, S.-Z. Qiao, *ACS Catal.* **2019**, *9*, 2902.
[19] L. Zhang, L.-X. Ding, G.-F. Chen, X. Yang, H. Wang, *Angew. Chem., Int. Ed.* **2019**, *58*, 2612.
[20] X. Cui, C. Tang, Q. Zhang, *Adv. Energy Mater.* **2018**, *8*, 1800369.
[21] Y. Wan, J. Xu, R. Lv, *Mater. Today* **2019**, *27*, 69.
[22] E. Skulason, T. Bligaard, S. Gudmundsdóttir, F. Studt, J. Rossmeisl, F. Abild-Pedersen, T. Vegge, H. Jonsson, J. K. Nørskov, *Phys. Chem. Chem. Phys.* **2012**, *14*, 1235.
[23] J. H. Montoya, C. Tsai, A. Vojvodic, J. K. Nørskov, *ChemSusChem* **2015**, *8*, 2180.
[24] C. Ling, X. Niu, Q. Li, A. Du, J. Wang, *J. Am. Chem. Soc.* **2018**, *140*, 14161.
[25] B. Qiao, A. Wang, X. Yang, L. F. Allard, Z. Jiang, Y. Cui, J. Liu, J. Li, T. Zhang, *Nat. Chem.* **2011**, *3*, 634.
[26] X. Chen, X. Zhao, Z. Kong, W.-J. Ong, N. Li, *J. Mater. Chem. A* **2018**, *6*, 21941.
[27] Z. Wei, Y. Zhang, S. Wang, C. Wang, J. Ma, *J. Mater. Chem. A* **2018**, *6*, 13790.
[28] C. Ling, X. Bai, Y. Ouyang, A. Du, J. Wang, *J. Phys. Chem. C* **2018**, *122*, 16842.

[29] C. Choi, S. Back, N.-Y. Kim, J. Lim, Y.-H. Kim, Y. Jung, *ACS Catal.* **2018**, *8*, 7517.

[30] Z. W. Chen, J. M. Yan, Q. Jiang, *Small Methods* **2019**, *3*, 1800291.

[31] Z. Geng, Y. Liu, X. Kong, P. Li, K. Li, Z. Liu, J. Du, M. Shu, R. Si, J. Zeng, *Adv. Mater.* **2018**, *30*, 1803498.

[32] H. Tao, C. Choi, L.-X. Ding, Z. Jiang, Z. Han, M. Jia, Q. Fan, Y. Gao, H. Wang, A. W. Robertson, S. Hong, Y. Jung, S. Liu, Z. Sun, *Chem* **2019**, *5*, 204.

[33] L. Han, X. Liu, J. Chen, R. Lin, H. Liu, F. Lü, S. Bak, Z. Liang, S. Zhao, E. Stavitski, J. Luo, R. R. Adzic, H. L. Xin. *Angew. Chem., Int. Ed.* **2019**, *58*, 2321.

[34] Q. Li, L. He, C. Sun, X. Zhang, *J. Phys. Chem. C* **2017**, *121*, 27563.

[35] L. M. Azofra, C. Sun, L. Cavallo, D. R. MacFarlane, *Chem. - Eur. J.* **2017**, *23*, 8275.

[36] C. Hering-Junghans, *Angew. Chem., Int. Ed.* **2018**, *57*, 6738.

[37] X. Yu, P. Han, Z. Wei, L. Huang, Z. Gu, S. Peng, J. Ma, G. Zheng, *Joule* **2018**, *2*, 1610.

[38] X. Mao, S. Zhou, C. Yan, Z. Zhu, A. Du, *Phys. Chem. Chem. Phys.* **2019**, *21*, 1110.

[39] S. Ji, Z. Wang, J. Zhao, *J. Mater. Chem. A* **2019**, *7*, 2392.

[40] Y. Cao, S. Deng, Q. Fang, X. Sun, C. Zhao, J. Zheng, Y. Gao, H. Zhuo, Y. Li, Z. Yao, *Nanotechnology* **2019**, *30*, 335403.

[41] M. Scardamaglia, M. Amati, B. Llorente, P. Mudimela, J.-F. Colomer, J. Ghijsen, C. Ewels, R. Snyders, L. Gregoratti, C. Bittencourt, *Carbon* **2014**, *77*, 319.

[42] S. Mukherjee, D. A. Cullen, S. Karakalos, K. Liu, H. Zhang, S. Zhao, H. Xu, K. L. More, G. Wang, G. Wu, *Nano Energy* **2018**, *48*, 217.

[43] Y. Liu, Y. Su, X. Quan, X. Fan, S. Chen, H. Yu, H. Zhao, Y. Zhang, J. Zhao, *ACS Catal.* **2018**, *8*, 1186.

[44] T. He, S. K. Matta, A. Du, *Phys. Chem. Chem. Phys.* **2019**, *21*, 1546.

[45] X. Liu, Y. Jiao, Y. Zheng, M. Jaroniec, S.-Z. Qiao, *J. Am. Chem. Soc.* **2019**, *141*, 9664.

[46] F. Yin, X. Lin, X. He, B. Chen, G. Li, H. Yin, *Mater. Lett.* **2019**, *248*, 109.

[47] L. Xia, X. Wu, Y. Wang, Z. Niu, Q. Liu, T. Li, X. Shi, A. M. Asiri, X. Sun, *Small Methods* **2019**, *3*, 1800251.

[48] J. Chen, H. Huang, L. Xia, H. Xie, L. Ji, P. Wei, R. Zhao, H. Chen, A. M. Asiri, X. Sun, *ChemistrySelect* **2019**, *4*, 3547.

[49] T. Wu, P. Li, H. Wang, R. Zhao, Q. Zhou, W. Kong, M. Liu, Y. Zhang, X. Sun, F. F. Gong, *Chem. Commun.* **2019**, *55*, 2684.

[50] Y. Tian, D. Xu, K. Chu, Z. Wei, W. Liu, *J. Mater. Sci.* **2019**, *54*, 9088.

[51] C. Lv, C. Yan, G. Chen, Y. Ding, J. Sun, Y. Zhou, G. Yu, *Angew. Chem., Int. Ed.* **2018**, *57*, 6073.

[52] G. Liu, Z. Cui, M. Han, S. Zhang, C. Zhao, C. Chen, G. Wang, H. Zhang, *Chem. - Eur. J.* **2019**, *25*, 5904.

[53] H. Xie, H. Wang, Q. Geng, Z. Xing, W. Wang, J. Chen, L. Ji, L. Chang, Z. Wang, J. Mao, *Inorg. Chem.* **2019**, *58*, 5423.

[54] S. Zhang, C. Zhao, Y. Liu, W. Li, J. Wang, G. Wang, Y. Zhang, H. Zhang, H. Zhao, *Chem. Commun.* **2019**, *55*, 2952.

[55] L. Yang, T. Wu, R. Zhang, H. Zhou, L. Xia, X. Shi, H. Zheng, Y. Zhang, X. Sun, *Nanoscale* **2019**, *11*, 1555.

[56] Z. Han, C. Choi, S. Hong, T.-S. Wu, Y.-L. Soo, Y. Jung, J. Qiu, Z. Sun, *Appl. Catal., B* **2019**, *257*, 117896.

[57] Y. Fang, Z. Liu, J. Han, Z. Jin, Y. Han, F. Wang, Y. Niu, Y. Wu, Y. Xu, *Adv. Energy Mater.* **2019**, *9*, 1803406.

[58] X. Cui, C. Tang, X. M. Liu, C. Wang, W. Ma, Q. Zhang, *Chem. - Eur. J.* **2018**, *24*, 18494.

[59] G. Zhang, Q. Ji, K. Zhang, Y. Chen, Z. Li, H. Liu, J. Li, J. Qu, *Nano Energy* **2019**, *59*, 10.

[60] Y. Abghoui, E. Skúlason, *J. Phys. Chem. C* **2017**, *121*, 6141.

[61] C. D. Zeinalipour-Yazdi, J. S. J. Hargreaves, C. R. A. Catlow, *J. Phys. Chem. C* **2018**, *122*, 6078.

[62] X. Ren, G. Cui, L. Chen, F. Xie, Q. Wei, Z. Tian, X. Sun, *Chem. Commun.* **2018**, *54*, 8474.

[63] L. Zhang, X. Ji, X. Ren, Y. Luo, X. Shi, A. M. Asiri, B. Zheng, X. Sun, *ACS Sustainable Chem. Eng.* **2018**, *6*, 9550.

[64] C. Lv, Y. Qian, C. Yan, Y. Ding, Y. Liu, G. Chen, G. Yu, *Angew. Chem., Int. Ed.* **2018**, *57*, 10246.

[65] I. Matanovic, F. H. Garzon, *Phys. Chem. Chem. Phys.* **2018**, *20*, 14679.

[66] X. Guo, S. Huang, *Electrochim. Acta* **2018**, *284*, 392.

[67] B. H. Suryanto, D. Wang, L. M. Azofra, M. Harb, L. Cavallo, R. Jalili, D. R. Mitchell, M. Chatti, D. R. MacFarlane, *ACS Energy Lett.* **2019**, *4*, 430.

[68] D. Chen, M. Qiao, Y. R. Lu, L. Hao, D. Liu, C. L. Dong, Y. Li, S. Wang, *Angew. Chem., Int. Ed.* **2018**, *57*, 8691.

[69] B. Liu, Y. Wang, H. Q. Peng, R. Yang, Z. Jiang, X. Zhou, C. S. Lee, H. Zhao, W. Zhang, *Adv. Mater.* **2018**, *30*, 1803144.

[70] Y. Wang, M.-m. Shi, D. Bao, F.-l. Meng, Q. Zhang, Y.-t. Zhou, K.-h. Liu, Y. Zhang, J.-z. Wang, Z.-w. Chen, D.-p. Liu, Z. Jiang, M. Luo, L. Gu, Q.-h. Zhang, X.-z. Cao, Y. Yao, M.-h. Shao, Y. Zhang, X.-B. Zhang, J. G. Chen, J.-m. Yan, Q. Jiang, *Angew. Chem., Int. Ed.* **2019**, *58*, 9464.

[71] Y. Li, Y. Kong, Y. Hou, B. Yang, Z. Li, L. Lei, Z. Wen, *ACS Sustainable Chem. Eng.* **2019**, *7*, 8853.

[72] T. Wang, X. Tian, Y. Yang, Y.-W. Li, J. Wang, M. Beller, H. Jiao, *J. Phys. Chem. C* **2016**, *120*, 2846.

[73] J. Qian, Q. An, A. Fortunelli, R. J. Nielsen, W. A. Goddard III, *J. Am. Chem. Soc.* **2018**, *140*, 6288.

[74] S. Hinrichsen, H. Broda, C. Gradert, L. Söncksen, F. Tuczek, *Annu. Rep., Sect. A: Inorg. Chem.* **2012**, *108*, 17.

[75] D. Yang, T. Chen, Z. Wang, *J. Mater. Chem. A* **2017**, *5*, 36.

[76] Y. Abghoui, E. Skúlason, *Catal. Today* **2017**, *286*, 78.

[77] H. Daims, E. V. Lebedeva, P. Pjevac, P. Han, C. Herbold, M. Albertsen, N. Jehmlich, M. Palatinszky, J. Vierheilig, A. Bulaev, *Nature* **2015**, *528*, 504.

[78] A. Hellman, E. Baerends, M. Biczysko, T. Bligaard, C. H. Christensen, D. Clary, S. v. Dahl, R. Van Harrevelt, K. Honkala, H. Jonsson, *J. Phys. Chem. B* **2006**, *110*, 17719.

[79] A. Ishikawa, T. Doi, H. Nakai, *J. Catal.* **2018**, *357*, 213.

[80] D. Bao, Q. Zhang, F. L. Meng, H. X. Zhong, M. M. Shi, Y. Zhang, J. M. Yan, Q. Jiang, X. B. Zhang, *Adv. Mater.* **2017**, *29*, 1604799.

[81] L. Wei, H. E. Karahan, S. Zhai, H. Liu, X. Chen, Z. Zhou, Y. Lei, Z. Liu, Y. Chen, *Adv. Mater.* **2017**, *29*, 1701410.

[82] J. M. V. Nsanzimana, Y. Peng, Y. Y. Xu, L. Thia, C. Wang, B. Y. Xia, X. Wang, *Adv. Energy Mater.* **2018**, *8*, 1701475.

[83] F. Hu, H. Wang, Y. Zhang, X. Shen, G. Zhang, Y. Pan, J. T. Miller, K. Wang, S. Zhu, X. Yang, *Small* **2019**, *15*, 1901020.

[84] H. Pang, J. Wang, X. Xiao, K. M. Pan, Y. Liu, S. Z. Wei, *J. Mater. Chem. A* **2019**, *7*, 4126.

[85] S. J. Li, D. Bao, M. M. Shi, B. R. Wulan, J. M. Yan, Q. Jiang, *Adv. Mater.* **2017**, *29*, 1700001.

[86] J. A. Farmer, C. T. Campbell, *Science* **2010**, *329*, 933.

[87] M. M. Shi, D. Bao, S. J. Li, B. R. Wulan, J. M. Yan, Q. Jiang, *Adv. Energy Mater.* **2018**, *8*, 1800124.

[88] H. Huang, L. Xia, R. Cao, Z. Niu, H. Chen, Q. Liu, T. Li, X. Shi, A. M. Asiri, X. Sun, *Chem. - Eur. J.* **2019**, *25*, 1914.

[89] G. Rao, X. Wang, Y. Wang, P. Wangyang, C. Yan, J. Chu, L. Xue, C. Gong, J. Huang, J. Xiong, *InfoMat* **2019**, *1*, 272.

[90] C. Tan, S. Xu, Z. Tan, L. Sun, J. Wu, T. Li, H. Peng, *InfoMat* **2019**, *1*, 390.

[91] J. Huang, Y. Sun, X. Du, Y. Zhang, C. Wu, C. Yan, G. Zou, W. Wu, R. Lu, Y. Li, J Xiong, *Adv. Mater.* **2018**, *30*, 1803367.

[92] W. Tian, H. Sun, L. Chen, P. Wangyang, X. Chen, J. Xiong, L. Li, *InfoMat* **2019**, *1*, 140.

[93] Y. Zhang, X. Xu, X. Fang, *InfoMat* **2019**, https://doi.org/10.1002/inf2.12035.

[94] J. Lin, P. Wang, H. Wang, C. Li, X. Si, J. Qi, J. Cao, Z. Zhong, W. Fei, J. Feng, *Adv. Sci.* **2019**, *6*, 1900246.

[95] J. Lv, S. Wu, Z. Tian, Y. Ye, J. Liu, C. Liang, *J. Mater. Chem. A* **2019**, *7*, 12627.

[96] P. Chen, N. Zhang, S. Wang, T. Zhou, Y. Tong, C. Ao, W. Yan, L. Zhang, W. Chu, C. Wu, Y. Xie, *Proc. Natl. Acad. Sci. USA* **2019**, *116*, 6635.

[97] S. Luo, X. Li, B. Zhang, Z. Luo, M. Luo, *ACS Appl. Mater. Interfaces* **2019**, *11*, 26891.

[98] Y. Yang, S. Wang, H. Wen, T. Ye, J. Chen, C. Li, M. Du, *Angew. Chem., Int. Ed.* **2019**, *58*, 15362.

[99] M. Peng, Y. Qiao, M. Luo, M. Wang, S. Chu, Y. Zhao, P. Liu, J. Liu, Y. Tan, *ACS Appl. Mater. Interfaces* **2019**, *11*, 40062.

[100] G. Zhang, H. Xu, Y. Li, C. Xiang, Q. Ji, H. Liu, Y. Qu, J. Li, *Adv. Sci.* **2019**, *6*, 1901627.

[101] B. H. Suryanto, C. S. Kang, D. Wang, C. Xiao, F. Zhou, L. M. Azofra, L. Cavallo, X. Zhang, D. R. MacFarlane, *ACS Energy Lett.* **2018**, *3*, 1219.

[102] X. Wang, X. Peng, Y. Zhang, J. Ni, C. Au, L. Jiang, *Front. Chem.* **2018**, *6*, 396.

[103] Y. Yao, S. Zhu, H. Wang, H. Li, M. Shao, *J. Am. Chem. Soc.* **2018**, *140*, 1496.